

# Continental basalts track secular cooling of the mantle and the onset of modern plate tectonics

**Qian Chen**

Institute of Oceanology, Chinese Academy of Sciences

**He Liu** (✉ [liuhe@qdio.ac.cn](mailto:liuhe@qdio.ac.cn))

Institute of Oceanology, Chinese Academy of Sciences <https://orcid.org/0000-0002-5588-0661>

**Tim Johnson**

Curtin University <https://orcid.org/0000-0001-8704-4396>

**Michael Hartnady**

School of Earth and Planetary Sciences, Curtin University

**Christopher Kirkland**

Curtin University <https://orcid.org/0000-0003-3367-8961>

**Yongjun Lu**

Geological Survey of Western Australia <https://orcid.org/0000-0002-6490-0679>

**Wei-Dong Sun**

CAS Key Lab of Marine Geology and Environment, Center of Deep Sea Research, Institute of Oceanology, Chinese Academy of Sciences, Qingdao 266071 <https://orcid.org/0000-0002-9003-9608>

---

## Article

**Keywords:** plate tectonics, mantle, temperature

**Posted Date:** April 22nd, 2021

**DOI:** <https://doi.org/10.21203/rs.3.rs-436896/v1>

**License:**   This work is licensed under a Creative Commons Attribution 4.0 International License.

[Read Full License](#)

---

---

1 **Continental basalts track secular cooling of the mantle and the onset**  
2 **of modern plate tectonics**

3  
4 Qian Chen<sup>1,2,3</sup>, He Liu<sup>1,2,3\*</sup>, Tim Johnson<sup>4</sup>, Michael Hartnady<sup>4</sup>, Christopher L  
5 Kirkland<sup>4</sup>, Yongjun Lu<sup>5,6</sup>, Wei-dong Sun<sup>1,2,3</sup>

6  
7 <sup>1</sup>*Center of Deep-Sea Research, Institute of Oceanology, Center for Ocean Mega-Science, Chinese*  
8 *Academy of Sciences, 7 Nanhai Road, Qingdao 266071, China*

9 <sup>2</sup>*Laboratory for Marine Mineral Resources, Qingdao National Laboratory for Marine Science and*  
10 *Technology, Qingdao 266237, China*

11 <sup>3</sup>*University of Chinese Academy of Sciences, Beijing 100094, China*

12 <sup>4</sup>*School of Earth and Planetary Sciences, Curtin University, GPO Box U1987, Perth, WA 6845,*  
13 *Australia*

14 <sup>5</sup>*Geological Survey of Western Australia, Department of Mines, Industry Regulation and Safety, 100*  
15 *Plain Street, East Perth, WA 6004, Australia*

16 <sup>6</sup>*Centre for Exploration Targeting and Australian Research Council Centre of Excellence for Core to*  
17 *Crust Fluid Systems (CCFS), University of Western Australia, Perth, WA 6009, Australia*

18  
19 \*Corresponding author. E-mail address: [liuhe@qdio.ac.cn](mailto:liuhe@qdio.ac.cn)

20

21

---

22 **The temperature of the convecting mantle exerts a first-order control on the**  
23 **tectonic behaviour of Earth's lithosphere. Although the mantle has likely been**  
24 **cooling since the Archaean eon (4.0–2.5 billion years ago), how mantle**  
25 **temperature evolved thereafter is poorly understood. Here, we apply a statistical**  
26 **analysis to secular changes in the alkali index (A.I. = whole-rock (Na<sub>2</sub>O +**  
27 **K<sub>2</sub>O)<sup>2</sup>/(SiO<sub>2</sub> – 38) as weight%) of intracontinental basalts globally to constrain**  
28 **the evolution of mantle potential temperature ( $T_p$ ) over the past billion years.**  
29 **During the early Neoproterozoic,  $T_p$  remained relatively constant at ~1450 °C**  
30 **until the Cryogenian (720 to 635 million years ago), when mantle temperature**  
31 **dropped by ~50 °C over <180 million years. This remarkable episode of cooling**  
32 **records the onset of modern-style plate tectonics, which has been suggested to**  
33 **have been triggered by a dramatic increase in the supply of sediments to**  
34 **lubricate trenches during thawing of the Snowball Earth.**

35

---

36 Whether or not some form of plate tectonics operated during the Archaean eon,  
37 what tectonic regime may have preceded it, and how Earth transitioned into the  
38 modern plate tectonic regime, characterised by deep subduction of cold oceanic  
39 plates, are fundamental questions that pertain to the development and maintenance of  
40 a habitable planet<sup>1-6</sup>. The composition, structure, and tectonic behaviour of the  
41 lithosphere, Earth's rigid outer rocky shell, are direct manifestations of the physical  
42 and chemical properties of the underlying convecting mantle (asthenosphere), of  
43 which temperature is a first-order control<sup>7-11</sup>. However, how mantle temperature has  
44 evolved with time is poorly understood<sup>12-15</sup>.

45 Continental basalts are mostly generated by adiabatic upwelling of the  
46 convecting mantle due to extension of the lithosphere, and thus provide a direct means  
47 of interrogating the thermal state of the mantle<sup>16-18</sup>. The degree of mantle melting ( $F$ )  
48 and the composition of continental basalts is largely a function of the temperature of  
49 the convecting mantle, which is commonly parameterised as mantle potential  
50 temperature ( $T_p$ ), the temperature a package of material would have at the surface if  
51 extrapolated along an adiabat assuming no melting<sup>18</sup>. The changing compositions of  
52 basaltic rocks through time suggest that Earth's upper mantle has been cooling since  
53 the Mesoarchean, consistent with thermal modelling<sup>5,14,19-21</sup>, although estimates of the  
54 peak  $T_p$  of the ambient mantle in the Archaean vary widely, from  $\sim 1400$  °C  
55 to  $>1700$  °C<sup>9,12,14,15</sup>. However, cooling of the mantle thereafter to a modern-day  
56 average of  $\sim 1350$  °C<sup>9,16,18</sup> has generally been considered to have been broadly  
57 linear<sup>5,9,14,17,19,22-24</sup>.

---

58 Plate tectonics, characterised by an interconnected network of narrow plate  
59 boundaries and widespread bimodal (paired) metamorphism, is generally regarded to  
60 have emerged at some time during the Mesoarchean to Paleoproterozoic<sup>2,6,8,24,25</sup>.  
61 However, the transition to the modern plate tectonic regime, characterised by  
62 relatively few plates and deep subduction of cold slabs, likely corresponds to the  
63 widespread appearance of ultra-high-pressure rocks and blueschists in the  
64 Neoproterozoic rock record at ~0.7 billion years ago (Ga)<sup>1,3,4,6,24</sup>. This transition has  
65 been argued to relate to the thawing of a Snowball Earth<sup>26</sup> and a consequent rapid  
66 increase in the supply of sediment to troughs that lubricated subduction<sup>27</sup>. If this  
67 geodynamic model is correct, the introduction of much larger volumes of cold  
68 lithosphere into the convecting mantle should have been associated with a broadly  
69 contemporaneous record of its cooling.

70 To test this hypothesis, here we perform a statistical analysis on a global  
71 geochemical database of intracontinental basalts to investigate variations in the  
72 pressure-temperature ( $P$ - $T$ ) conditions of mantle melting and constrain the secular  
73 evolution in  $T_P$  over the past billion years. The data indicate a rapid drop in  $T_P$  at  
74 around 0.7 Ga, which we interpret to correspond to the onset of modern-style plate  
75 tectonics, concomitant with an increase in the volume of subducted cold oceanic  
76 lithosphere in the Neoproterozoic.

## 77 **Results**

78 **Subcontinental mantle melting.** Partial melting of the mantle occurs over a range of

---

79 depths (the melting column). The base of the melting column is defined by the  
80 intersection of the peridotite solidus and the convective geotherm ( $T_P$ ) at pressure  $P_0$ ,  
81 while the top is constrained by the intersection of the peridotite solidus and the  
82 conductive geotherm at pressure  $P_f$  (Fig. 1). Recent work has shown that the  
83 compositions of modern (Cenozoic) intracontinental basalts are primarily controlled  
84 by the final (minimum) pressure of melting or equilibration ( $P_f$ )<sup>17,28</sup>. Importantly,  $P_f$  is  
85 a direct function of  $T_P$ , such that a reduction in  $T_P$  results in an increase in  $P_f$ <sup>18,29</sup> (Fig.  
86 1) and a decrease in the degree of mantle melting ( $F$ )<sup>17,30</sup>.

87 The total alkali ( $\text{Na}_2\text{O} + \text{K}_2\text{O}$  in wt%) and silica ( $\text{SiO}_2$  in wt%) contents of  
88 basaltic rocks are strongly related to the pressure ( $P$ ) and temperature ( $T$ ) of final  
89 melting or equilibration<sup>17,30</sup>. Using a pMELTS simulation<sup>31</sup>, we model the total alkali  
90 and silica content of basaltic melts through isobaric batch melting using the major  
91 element composition of primitive mantle as the source<sup>32</sup> (Fig. 2). We initialize the  
92 mantle compositions with 0.1 wt% and 0.3 wt%  $\text{H}_2\text{O}$ , to account for inferred water  
93 contents (0.2–0.3 wt%  $\text{H}_2\text{O}$ ) in the mantle transition zone associated with modern  
94 intracontinental volcanism<sup>33</sup> and to account for the likelihood that Precambrian  
95 subcontinental mantle may have been less hydrated<sup>34</sup>.

96 In the models (Fig. 2), the total alkali content of melt shows a positive  
97 correlation with pressure and a negative correlation with temperature (and  $F$ ), whereas  
98 silica contents decrease strongly with increasing pressure, but are less sensitive to  
99 temperature. Thus, basaltic rocks with relatively high total alkalis and low silica  
100 contents reflect a low degree of mantle melting under low-temperature and/or high-

---

101 pressure conditions. These predictions are consistent with the measured compositions  
102 of basalts (volcanic rocks with 45–55 wt% SiO<sub>2</sub>) extracted from the EarthChem  
103 database ([www.earthchem.org/portal](http://www.earthchem.org/portal))<sup>35</sup>. Relative to modern arc basalts from the  
104 western Pacific, modern (<10 Ma, Ma = million years ago) intracontinental basalts  
105 from eastern Asia contain relatively higher total alkalis and lower silica contents  
106 (Supplementary Fig. 1), consistent with the fact that intracontinental basalts reflect  
107 lower degrees of melting of a less hydrated mantle at higher  $P_f$ <sup>36</sup>. Relative to modern  
108 intracontinental basalts, Proterozoic and Archaean basalts (Supplementary Fig. 2b and  
109 c, respectively) have lower total alkalis but higher silica contents, consistent with their  
110 production at higher  $T_P$ <sup>17,30</sup>.

111

112 **Secular variations in the alkali index of basalts.** To account for variations in both  
113 alkali and silica contents, we develop a new parameter, the alkali index (A.I. = (Na<sub>2</sub>O  
114 + K<sub>2</sub>O)<sup>2</sup>/(SiO<sub>2</sub> – 38)), as a proxy for the  $P$ – $T$  conditions of mantle melting (Fig. 2).

115 We apply this parameter to a compilation of whole-rock compositions of sodic  
116 (Na<sub>2</sub>O/K<sub>2</sub>O >1) intracontinental basalts globally to constrain the thermal evolution of  
117 the mantle over the last billion years (see Methods). Crustal thickness exerts a primary  
118 control on Sr/Y through the stabilization or destabilization of the principal Sr-bearing  
119 (plagioclase) and Y-bearing (garnet and/or amphibole) minerals. Based on the  
120 compositions of modern (<10 Ma) basalts from known tectonic settings, the  
121 compilation is filtered to exclude those basalts formed in arcs and large igneous  
122 provinces by considering only samples with Sr/Y > 25 (Supplementary Fig. 3), which

---

123 reflects the relatively high pressure at which they formed. To eliminate the possible  
124 effects of alteration or metamorphism, we have also applied a filter to all basalt data  
125 based on plots of A.I. versus La (which is resistant to alteration or metamorphism) in  
126 intracontinental basalts younger than 10 Ma (see Methods and Supplementary Fig. 4a  
127 and 4b). We use this filtered dataset to calculate the average A.I. for the  
128 intracontinental basalts with known different ages to obtain the temporal variation of  
129 A.I. over the past billion years (Fig. 3a and Supplementary Fig. 4c).

130 The average A.I., Na<sub>2</sub>O and K<sub>2</sub>O contents for the high-Sr/Y intracontinental  
131 basalts from 1.0 Ga (1000 Ma) to the present day is shown in Fig. 3a and 3b, along  
132 with the secular trends for average La/Sm ratios and Th concentrations (Fig. 3c and  
133 3d). Notably, these values are relatively constant before the Cryogenian (720–635 Ma;  
134 pale blue band in Fig. 3) but increase thereafter. This increase is particularly  
135 pronounced for A.I., for which values of 1.2 before ~750 Ma increase during the  
136 Cryogenian to Ediacaran to a value of around 2.0 at ~550 Ma (Fig. 3a).

137

## 138 **Discussion**

139 Considering that the A.I. of intracontinental basalts correlates positively with  $P_f$   
140 and negatively with  $T_p$ , we suggest that the trend in A.I. tracks the evolution of  $T_p$ .  
141 Although fractional crystallization and interaction with crust during magma ascent  
142 likely affects the A.I. of basalts, in the absence of changes in the degree of fractional  
143 crystallization or crustal contamination through time, such influences will result in a  
144 systematic offset<sup>17</sup>. Moreover, if the rise in A.I. since the Cryogenian (Fig. 3a) was

---

145 caused by a gradual increase in crustal contamination, Nb/Th and Nb/Rb ratios in the  
146 basalts should decrease through time due to low Nb/Th and Nb/Rb ratios in  
147 continental crust<sup>37</sup>. However, no such trends are observed (Supplementary Fig. 5).

148 Another potential concern is that the data may reflect increasing CO<sub>2</sub> contents in  
149 the mantle due to the subduction of carbonates, which have been shown to decrease  
150 the SiO<sub>2</sub> content of melt at 3 GPa but to have little influence on Na<sub>2</sub>O contents<sup>38</sup>  
151 (Supplementary Fig. 6). However, the SiO<sub>2</sub> contents of intracontinental basalts do not  
152 decrease around the Cryogenian–Ediacaran (Supplementary Fig. 7), whereas Na<sub>2</sub>O  
153 contents increase significantly from ~2.8 wt% at 750 Ma to ~3.6 wt% at 550 Ma (Fig.  
154 3b). For the melting of the carbonated mantle at a lower pressure (<2 GPa), a  
155 pMELTS model shows that an increase of CO<sub>2</sub> in mantle peridotite has a negligible  
156 influence on the total alkali and silica contents of the melt (Fig. 4), consistent with  
157 existing experimental data<sup>39</sup>. Given the above relationships, we interpret the rapid  
158 elevation of average A.I. in global-scale intracontinental basalts during the  
159 Cryogenian–Ediacaran as caused by a global episode of enhanced mantle cooling.  
160 To facilitate a comparison of A.I. values in intracontinental basalts (Fig. 3a) with  
161 mantle temperature, we compare our data with existing estimates of  $T_P$ . Extrapolating  
162 the trend of compositions of non-arc basalts interpreted to be primary melts of the  
163 mantle<sup>14,34</sup> gives an estimated  $T_P$  of ~1480 °C at 1.0 Ga, comparable to existing  
164 estimates (1380–1520 °C) based on geochemical constraints<sup>23</sup>, but higher than those  
165 (~1400 – 1430 °C) based on simple heat loss parameterisation<sup>21</sup>. Assuming an  
166 intermediate value for  $T_P$  of 1450 °C at 1.0 Ga and 1350 °C today (Supplementary

---

167 Fig. 8), our results suggest that  $T_P$  decreased by around 50 °C to 1400 °C during the  
168 Cryogenian–Ediacaran (Fig. 5a). During the Phanerozoic,  $T_P$  fluctuated but decreased  
169 gradually.

170 During the billion years between the Mesoarchean and the Huronian glaciation (2.45–  
171 2.22 Ga)<sup>40</sup>, the geodynamic regime on Earth likely transited from a deformable  
172 stagnant-lid to some form of plate tectonics, although subduction was likely episodic  
173 rather than continuous<sup>2,3,25,41</sup>. Sometime thereafter, subduction became continuous<sup>25</sup>,  
174 ultimately leading to the formation of the supercontinent Columbia<sup>42,43</sup>. It is generally  
175 accepted that the onset of modern-style plate tectonics occurred during the  
176 Neoproterozoic, consistent with the widespread appearance of low- $T/P$  metamorphic  
177 rocks ( $T/P < 375$  °C/GPa, Fig 5c)<sup>1</sup>, including blueschists and ultrahigh-pressure  
178 metamorphic rocks, reflecting cold subduction of the oceanic lithosphere to depths  
179 exceeding 100 km<sup>1,4,6</sup>. This transition has been interpreted to have been triggered by a  
180 rapid increase in the supply of sediment to trenches following thawing of the  
181 Neoproterozoic Snowball Earth, in which the sediments acted as a lubricant for  
182 subduction<sup>27</sup>. The introduction of large volumes of cold oceanic lithosphere into the  
183 mantle during this transition would have greatly enhanced the cooling rate of the  
184 mantle, consistent with our calculation of a decline in  $T_P$  by ~50 °C from the  
185 beginning of the Cryogenian to the end of the Ediacaran (~720–541 Ma),  
186 corresponding to a mean cooling rate of ~0.3 °C/million years (Fig. 5a). Such a  
187 dramatic change in the thermal state of the mantle in the Neoproterozoic accords with  
188 secular variations in the temperature ( $T_g$ ) of formation of basalts derived from

---

189 depleted mantle<sup>44</sup>, which also show a decrease of >50 °C after the Cryogenian (Fig.  
190 5b).

191 During the Phanerozoic, our model suggests that  $T_P$  decreased more gradually to  
192 reach the current average of ~1350 °C. This likely reflects a reduced subduction rate  
193 due to the assembly of the supercontinent Pannotia/Gondwana<sup>45,46</sup> at the end of the  
194 Neoproterozoic, as tracked by widespread Pan-African orogenesis<sup>47,48</sup>. Assembly of  
195 Pannotia/Gondwana would have provided thermal insulation below the amalgamated  
196 supercontinent, further slowing mantle cooling.<sup>49,50</sup> A slow-down in subduction after  
197 Pan-African orogenesis may correspond to the exhaustion of sediment supply as  
198 Rodinia reached its peneplanation surface<sup>27</sup>.

199

## 200 **Methods**

201 **Simulation of mantle melting.** Simulations used the pMELTS (v5.6.1)  
202 software<sup>35</sup> to constrain the total alkali (Na<sub>2</sub>O + K<sub>2</sub>O, wt%) and silica contents (SiO<sub>2</sub>,  
203 wt%) of magmas generated via partial melting of the mantle. The modelled major  
204 element composition is the primitive mantle composition of McDonough and Sun<sup>32</sup>  
205 with 0.1-0.3 wt% H<sub>2</sub>O or 0.1-0.3 wt% CO<sub>2</sub>. Calculations assumed an isobaric batch  
206 mantle melting model from solidus to liquidus at pressures between 1.0 and 2.0 GPa  
207 and temperature from 1000 to 1600 °C (Fig. 2 and 4).

208 **Data preparation and filtering.** Geochemical data for all volcanic rocks were  
209 compiled from the EarthChem database ([www.earthchem.org/portal](http://www.earthchem.org/portal)). Plutonic rocks  
210 were not considered due to the likely effects of fractionation and assimilation<sup>51</sup>. All

---

211 oceanic samples were excluded from the compilation to focus on intracontinental  
212 basalts. Rocks with ages from >3.2 Ga are too scarce in the compilation for  
213 meaningful discussion and are not considered. Phanerozoic rocks with age uncertainty  
214 greater than 50 Myr (million years) and Precambrian rocks with age uncertainty  
215 greater than 100 Myr were omitted to ensure temporal accuracy. Kimberlites and  
216 carbonatites were also not considered as they are rare and may have been  
217 oversampled. The dataset containing 43,836 individual basaltic rocks (volcanic rocks  
218 with 45–55 wt% SiO<sub>2</sub>) with ages spanning 3.2–0 Ga is provided in Supplementary  
219 Data 1 (Supplementary Fig. 9).

220 We focus on the compositional variability of intracontinental basalts through  
221 time, as the Na<sub>2</sub>O and K<sub>2</sub>O contents in arc volcanic rocks are strongly influenced by  
222 fluid-mediated metasomatism (Supplementary Fig. 1). To filter the data for  
223 intracontinental basalts, we compared the Sr/Y of basalts from the modern  
224 intracontinental, arc, and typical large igneous province (LIP) settings. Given that  
225 intracontinental basalts commonly form under high melting pressures, most arc and  
226 LIP basalts can be excluded by removing samples with Sr/Y ≤ 25 (Supplementary Fig.  
227 3). The intracontinental basalts commonly include sodic and potassic groups  
228 according to their Na<sub>2</sub>O/K<sub>2</sub>O ratio<sup>36</sup>. The sodic basalts are interpreted as magmas  
229 produced by low-degree mantle melting, whereas potassic magmas may be related to  
230 the melting of metasomatised mantle<sup>36</sup>. We use Na<sub>2</sub>O/K<sub>2</sub>O < 1 as a criterion to  
231 exclude potassic basalts<sup>36</sup>. The filtered dataset of intracontinental basalts contains  
232 geochemical analyses of 8,525 samples.

---

233       **Plots and spatial density contours.** The sample location and total alkali  
234 contents for <10 Ma east Asia basalts were plotted using ArcGIS (v.10.2). These  
235 samples were selected as their current position is likely a good representation of the  
236 tectonic setting in which they formed. Density contours of total alkali vs. silica  
237 content (Supplementary Figs. 1 and 2) were generated using Surfer (v.12) through the  
238 Data Metrics function. The grid size for both the x-axis and y-axis was set at 1 wt%.

239       **Temporary variations of A.I.** To characterize the evolution of the thermal state  
240 of the upper mantle throughout Earth's history, we extracted the bulk compositions of  
241 basaltic rocks ( $\text{SiO}_2 = 45\text{--}55$  wt%) and accessed the data for secular variation in the  
242 degree of mantle melting. Higher total alkalis in rocks with the same silica contents  
243 usually indicate higher alkalinity. To account for this, we define a new variable, the  
244 alkalinity index (A.I.) in mafic rocks, where  $\text{A.I.} = (\text{K}_2\text{O} + \text{Na}_2\text{O})^2 / (\text{SiO}_2 - 38)$ , as a  
245 proxy for the  $T$ - $P$  conditions of mantle melting.

246       Old basalts may have undergone different degrees of alteration and  
247 metamorphism after their formation, which could have affected their composition. As  
248 such, we used La concentration in rocks to control data quality. Like A.I., La is a  
249 typical incompatible element whose concentrations in the melt should be negatively  
250 correlated with the degree of melting but which is unaffected by alteration or  
251 metamorphism. Plots of  $\log_{10}$  A.I. vs.  $\log_{10}$  La in young intracontinental basalts (<10  
252 Ma) show A.I. to correlate positively with La concentrations (Supplementary Fig. 4a).  
253 In a plot of  $\log_{10}$  A.I. vs.  $\log_{10}$  La of all intracontinental basalts (Supplementary Fig.  
254 4b), we excluded any samples outside the 3 s.d. (standard deviation) envelope of the

---

255 mean, which effectively precludes strongly altered samples adversely influencing  
256 temporal trends (Fig. 3a and Supplementary Fig. 4c).

257 The secular trends of average A.I., Na<sub>2</sub>O, K<sub>2</sub>O and Th concentrations, and La/Sm  
258 ratios in a global dataset of intracontinental basalts through time (Fig. 3) were created  
259 using MATLAB (R2014a). The means and standard errors of the means (s.e.m.) were  
260 calculated by Bootstrap resampling with 10,000 iterations. A central moving average  
261 smoothing with a 200-Myr (or 300-Myr when the data are too scattered) sample  
262 window was applied to highlight the main temporal trend. Outlier elimination was  
263 performed on each sample window (10<sup>th</sup>-90<sup>th</sup> percentile). The step width was set at 50  
264 Myr.

265 **Model of  $T_P$ .** Although the A.I. in intracontinental basalts cannot be used to  
266 estimate the  $T_P$  of the ambient mantle, it could reflect the relative variations of the  $T$ -  
267  $P$  conditions of subcontinental mantle melting. As such, we used the A.I. trend of  
268 intracontinental basalts to modify the previously estimated model of the  $T_P$ . The  $T_P$  of  
269 the ambient mantle at 1000 Ma has previously been estimated in the range of 1400–  
270 1480 °C<sup>14,21,23,34</sup>. Here we adopt an intermediate value of 1450°C for 1000 Ma and  
271 regard 1350°C as the present-day  $T_P$ . A Monte Carlo simulation was applied to  
272 generate a model of  $T_P$  by: 1) randomly synthesizing one group of Gaussian-  
273 distributed data (2,000 individual values) for each A.I. measure of global  
274 intracontinental basalts (Fig. 3a). The mean and standard deviation of the simulated  
275 Gaussian-distributed data was equal to the mean and s.e.m. of the A.I. content,  
276 respectively, then a total of 42,000 synthetic A.I. values were obtained. 2) Each

---

277 synthetic A.I. was converted into a  $T_P$  using the fitting function shown in  
278 Supplementary Fig. 8. The mean and two standard deviations of the  $T_P$  for every 40-  
279 Myr age bin was calculated (Fig. 5a).

280

### 281 **Data availability**

282 The datasets used in this study are provided as Supplementary Dataset 1. The  
283 source data underlying Figs. 3 and 5, and Supplementary Figs. 5 and 7 is provided as  
284 a Source Data file. Supplementary Dataset 1 has also been deposited in the GitHub  
285 repository (<https://github.com/CodrIocas/Cooling.git>).

286

### 287 **Code availability**

288 The computer codes used in this study are provided as Supplementary  
289 Information. All the relevant codes are freely available in GitHub at  
290 <https://github.com/CodrIocas/Cooling.git>. The MATLAB codes are provided under a  
291 GNU GPL v2.0 open-source license.

292

### 293 **Acknowledgements**

294 This study was supported by the Strategic Priority Research Program of the Chinese  
295 Academy of Sciences (XDB18020102) and the National Natural Science Foundation  
296 of China (42073011). T.J. acknowledges support from Open fund GPMR201903 from  
297 the State Key Laboratory of Geological Processes and Mineral Resources, China  
298 University of Geosciences, Wuhan. Y.L. publishes with the permission of the

---

299 Executive Director, Geological Survey of Western Australia.

300

301 **Author contributions**

302 H.L conceived this study. HL. processed the data and conducted the MATLAB  
303 coding. M.H. and C.L.K. verified the results. T.J., H.L., and Q.C. wrote the  
304 manuscript with contributions from all co-authors. All authors participated in  
305 discussions relating to the original and revised manuscript.

306

307 **Competing interests:** The authors declare no competing interests.

308

309 **Additional Information**

310 Correspondence and requests for materials should be addressed to H.L.

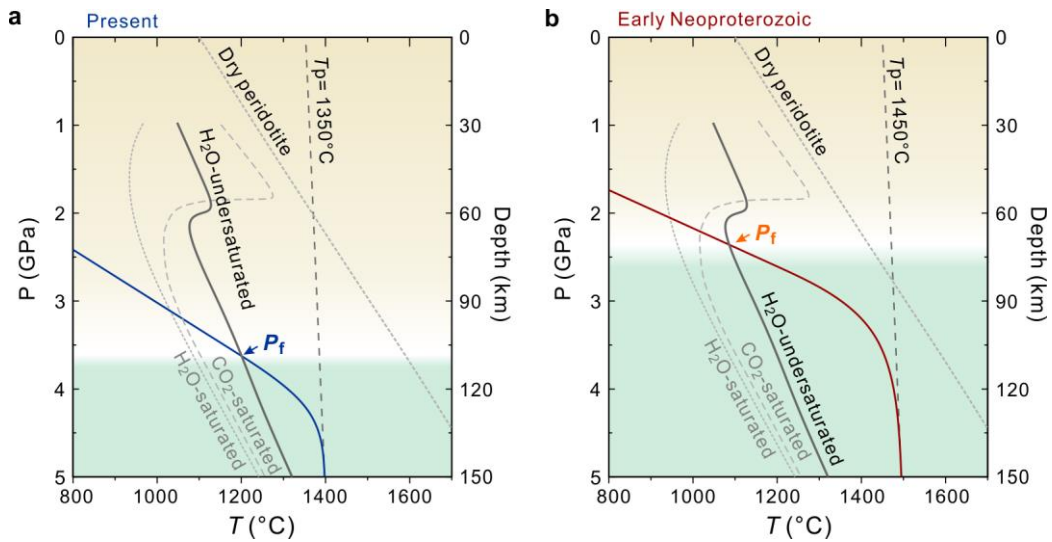
---

311 **REFERENCES**

- 312 1. Brown, M. & Johnson, T. Metamorphism and the evolution of subduction on Earth. *American*  
313 *Mineralogist* **104**, 1065-1082 (2019).
- 314 2. Brown, M., Johnson, T. & Gardiner, N.J. Plate Tectonics and the Archean Earth. *Annual Review*  
315 *of Earth and Planetary Sciences* **48**(2020).
- 316 3. Cawood, P.A. *et al.* Geological archive of the onset of plate tectonics. *Philosophical*  
317 *Transactions of the Royal Society a-Mathematical Physical and Engineering Sciences*  
318 **376**(2018).
- 319 4. Hawkesworth, C.J., Cawood, P.A., Dhuime, B. & Kemp, T.I.S. Earth's Continental Lithosphere  
320 Through Time. *Annual Review of Earth and Planetary Sciences* **45**, 169-198 (2017).
- 321 5. Korenaga, J. Initiation and Evolution of Plate Tectonics on Earth: Theories and Observations.  
322 in *Annual Review of Earth and Planetary Sciences, Vol 41*, Vol. 41 (ed. Jeanloz, R.) 117-151  
323 (Annual Reviews, Palo Alto, 2013).
- 324 6. Stern, R.J. The evolution of plate tectonics. *Philosophical Transactions of the Royal Society a-*  
325 *Mathematical Physical and Engineering Sciences* **376**(2018).
- 326 7. Bercovici, D. The generation of plate tectonics from mantle convection. *Earth and Planetary*  
327 *Science Letters* **205**, 107-121 (2003).
- 328 8. Lenardic, A. The diversity of tectonic modes and thoughts about transitions between them.  
329 *Philosophical Transactions of the Royal Society A: Mathematical, Physical and Engineering*  
330 *Sciences* **376**, 20170416 (2018).
- 331 9. Putirka, K. Rates and styles of planetary cooling on Earth, Moon, Mars, and Vesta, using new  
332 models for oxygen fugacity, ferric-ferrous ratios, olivine-liquid Fe-Mg exchange, and mantle  
333 potential temperature. *American Mineralogist* **101**, 819-840 (2016).
- 334 10. Rolf, T., Coltice, N. & Tackley, P. Linking continental drift, plate tectonics and the thermal state  
335 of the Earth's mantle. *Earth and Planetary Science Letters* **351**, 134-146 (2012).
- 336 11. Tackley, P.J. Mantle convection and plate tectonics: Toward an integrated physical and chemical  
337 theory. *Science* **288**, 2002-2007 (2000).
- 338 12. Aulbach, S. & Arndt, N.T. Eclogites as palaeodynamic archives: evidence for warm (not hot)  
339 and depleted (but heterogeneous) Archaean ambient mantle. *Earth and Planetary Science*  
340 *Letters* **505**, 162-172 (2019).
- 341 13. Herzberg, C. Origin of high-Mg bimineralic eclogite xenoliths in kimberlite: a comment on a  
342 paper by Aulbach and Arndt (2019). *Earth and Planetary Science Letters* **510**, 231-233 (2019).
- 343 14. Herzberg, C., Condie, K. & Korenaga, J. Thermal history of the Earth and its petrological  
344 expression. *Earth and Planetary Science Letters* **292**, 79-88 (2010).
- 345 15. Nisbet, E., Cheadle, M., Arndt, N. & Bickle, M. Constraining the potential temperature of the  
346 Archaean mantle: a review of the evidence from komatiites. *Lithos* **30**, 291-307 (1993).
- 347 16. Herzberg, C. *et al.* Temperatures in ambient mantle and plumes: Constraints from basalts,  
348 picrites, and komatiites. *Geochemistry, Geophysics, Geosystems* **8**(2007).
- 349 17. Keller, B. & Schoene, B. Plate tectonics and continental basaltic geochemistry throughout Earth  
350 history. *Earth and Planetary Science Letters* **481**, 290-304 (2018).
- 351 18. McKenzie, D. & Bickle, M. The volume and composition of melt generated by extension of the  
352 lithosphere. *Journal of petrology* **29**, 625-679 (1988).
- 353 19. Davies, G.F. Effect of plate bending on the Urey ratio and the thermal evolution of the mantle.  
354 *Earth and Planetary Science Letters* **287**, 513-518 (2009).

- 
- 355 20. Korenaga, J. Urey ratio and the structure and evolution of Earth's mantle. *Reviews of Geophysics*  
356 **46**(2008).
- 357 21. Labrosse, S. & Jaupart, C. Thermal evolution of the Earth: Secular changes and fluctuations of  
358 plate characteristics. *Earth and Planetary Science Letters* **260**, 465-481 (2007).
- 359 22. Christensen, U.R. Thermal Evolution Models for the Earth. *Journal of Geophysical Research-  
360 Solid Earth and Planets* **90**, 2995-3007 (1985).
- 361 23. Ganne, J. & Feng, X. Primary magmas and mantle temperatures through time. *Geochemistry,  
362 Geophysics, Geosystems* **18**, 872-888 (2017).
- 363 24. Holder, R.M., Viete, D.R., Brown, M. & Johnson, T.E. Metamorphism and the evolution of plate  
364 tectonics. *Nature* (2019).
- 365 25. Liu, H., Sun, W.-d., Zartman, R. & Tang, M. Continuous plate subduction marked by the rise of  
366 alkali magmatism 2.1 billion years ago. *Nature Communications* **10**, 3408 (2019).
- 367 26. Hoffman, P.F., Kaufman, A.J., Halverson, G.P. & Schrag, D.P. A Neoproterozoic snowball earth.  
368 *science* **281**, 1342-1346 (1998).
- 369 27. Sobolev, S.V. & Brown, M. Surface erosion events controlled the evolution of plate tectonics  
370 on Earth. *Nature* **570**, 52-57 (2019).
- 371 28. Guo, P., Niu, Y., Sun, P., Gong, H. & Wang, X. Lithosphere thickness controls continental basalt  
372 compositions: An illustration using Cenozoic basalts from eastern China. *Geology* **48**, 128-133  
373 (2020).
- 374 29. Vanderhaeghe, O., Guergouz, C., Fabre, C., Duchêne, S. & Baratoux, D. Secular cooling and  
375 crystallization of partially molten Archaean continental crust over 1 Ga. *Comptes Rendus  
376 Geoscience* **351**, 562-573 (2019).
- 377 30. Keller, C.B. & Schoene, B. Statistical geochemistry reveals disruption in secular lithospheric  
378 evolution about 2.5 Gyr ago. *Nature* **485**, 490-493 (2012).
- 379 31. Ghiorso, M.S., Hirschmann, M.M., Reiners, P.W. & Kress, V.C. The pMELTS: A revision of  
380 MELTS for improved calculation of phase relations and major element partitioning related to  
381 partial melting of the mantle to 3 GPa. *Geochemistry Geophysics Geosystems* **3**, 36 (2002).
- 382 32. McDonough, W.F. & Sun, S.S. The Composition of the Earth. *Chemical Geology* **120**, 223-253  
383 (1995).
- 384 33. Yang, J. & Faccenda, M. Intraplate volcanism originating from upwelling hydrous mantle  
385 transition zone. *Nature* **579**, 88-91 (2020).
- 386 34. Korenaga, J. Thermal evolution with a hydrating mantle and the initiation of plate tectonics in  
387 the early Earth. *Journal of Geophysical Research: Solid Earth* **116**(2011).
- 388 35. EarthChem. Portal Search. Vol. 2017 (IEDA, 2017).
- 389 36. Farmer, G.L. 4.3 - Continental Basaltic Rocks. in *Treatise on Geochemistry (Second Edition)*  
390 (eds. Holland, H.D. & Turekian, K.K.) 75-110 (Elsevier, Oxford, 2014).
- 391 37. Rudnick, R.L. & Gao, S. 4.1 - Composition of the Continental Crust. in *Treatise on  
392 Geochemistry (Second Edition)* (eds. Holland, H.D. & Turekian, K.K.) 1-51 (Elsevier, Oxford,  
393 2014).
- 394 38. Dasgupta, R., Hirschmann, M.M. & Smith, N.D. Partial Melting Experiments of Peridotite +  
395 CO<sub>2</sub> at 3 GPa and Genesis of Alkalic Ocean Island Basalts. *Journal of Petrology* **48**, 2093-2124  
396 (2007).
- 397 39. Falloon, T.J. & Green, D.H. The solidus of carbonated, fertile peridotite. *Earth and Planetary  
398 Science Letters* **94**, 364-370 (1989).

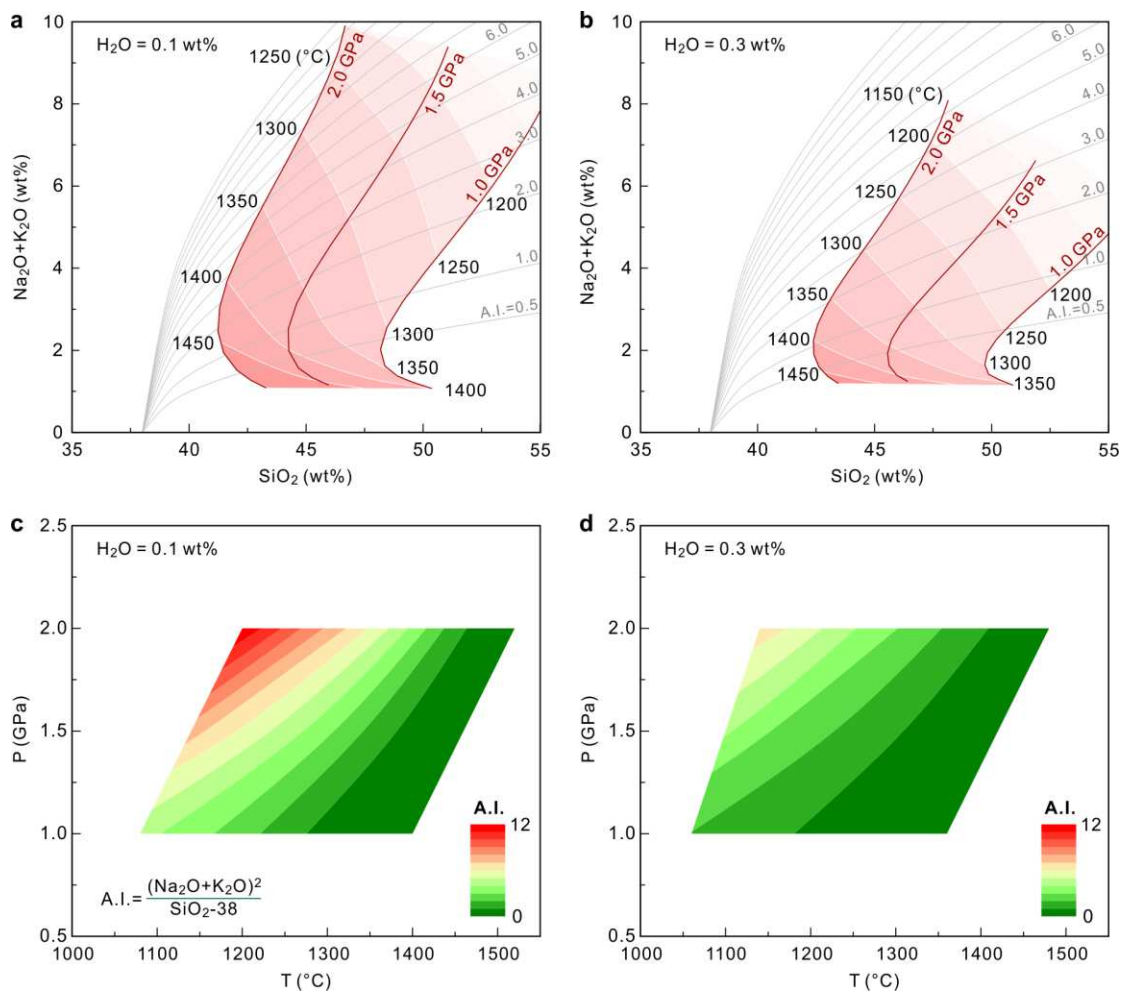
- 
- 399 40. Bekker, A. & Holland, H.D. Oxygen overshoot and recovery during the early Paleoproterozoic.  
400 *Earth and Planetary Science Letters* **317**, 295-304 (2012).
- 401 41. Moyer, J.-F. & Van Hunen, J. Short-term episodicity of Archaean plate tectonics. *Geology* **40**,  
402 451-454 (2012).
- 403 42. Cawood, P.A. & Hawkesworth, C.J. Earth's middle age. *Geology* **42**, 503-506 (2014).
- 404 43. Zhao, G.C., Sun, M., Wilde, S.A. & Li, S.Z. A Paleo-Mesoproterozoic supercontinent: assembly,  
405 growth and breakup. *Earth-Science Reviews* **67**, 91-123 (2004).
- 406 44. Condie, K.C., Aster, R.C. & van Hunen, J. A great thermal divergence in the mantle beginning  
407 2.5 Ga: Geochemical constraints from greenstone basalts and komatiites. *Geoscience Frontiers*  
408 **7**, 543-553 (2016).
- 409 45. Murphy, J. *et al.* Pannotia: In defence of its existence and geodynamic significance. *Geological*  
410 *Society, London, Special Publications* **503**(2020).
- 411 46. Nance, R.D. & Murphy, J.B. Supercontinents and the case for Pannotia. *Geological Society,*  
412 *London, Special Publications* **470**, 65 (2019).
- 413 47. Silver, P.G. & Behn, M.D. Intermittent plate tectonics? *Science* **319**, 85-88 (2008).
- 414 48. Spencer, C.J., Hawkesworth, C., Cawood, P.A. & Dhuime, B. Not all supercontinents are  
415 created equal: Gondwana-Rodinia case study. *Geology* **41**, 795-798 (2013).
- 416 49. Van Avendonk, H.J.A., Davis, J.K., Harding, J.L. & Lawver, L.A. Decrease in oceanic crustal  
417 thickness since the breakup of Pangaea. *Nature Geoscience* **10**, 58-61 (2017).
- 418 50. Jérôme, G., Xiaojun, F., Patrice, R. & Vincent De, A. Statistical petrology reveals a link between  
419 supercontinents cycle and mantle global climate. *American Mineralogist* **101**, 2768-2773 (2016).
- 420 51. Keller, C.B., Schoene, B., Barboni, M., Samperton, K.M. & Husson, J.M. Volcanic–plutonic  
421 parity and the differentiation of the continental crust. *Nature* **523**, 301 (2015).
- 422



424

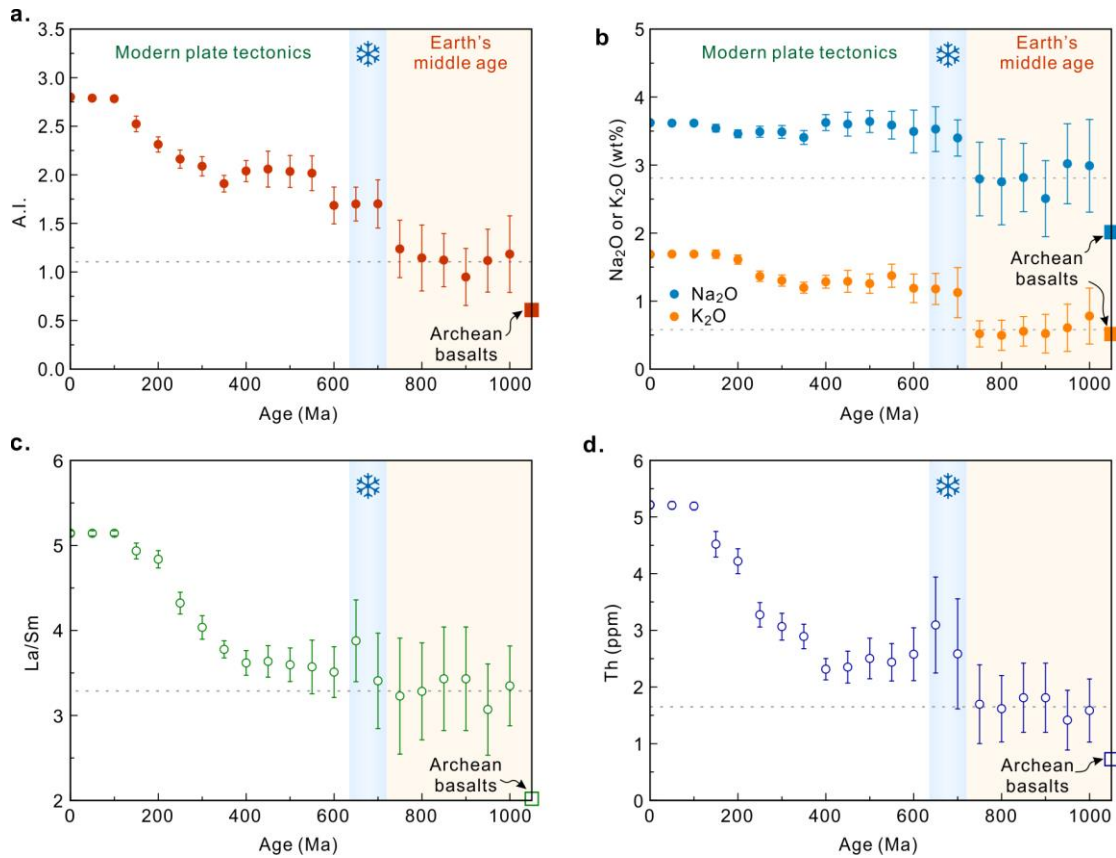
425 **Fig. 1** Relation between the pressure of the final melting ( $P_f$ ) of the mantle and  
 426 the potential temperature ( $T_P$ ) of the adiabatic mantle. The solidus of dry  
 427 peridotite, H<sub>2</sub>O-undersaturated, H<sub>2</sub>O-saturated and CO<sub>2</sub>-saturated pyrolite<sup>39</sup> are shown  
 428 with their labels. **a.** A schematic model showing the depth of  $P_f$  at present ( $T_P$   
 429 =1350°C). **b.** A schematic model showing the depth of  $P_f$  in the Early Neoproterozoic  
 430 ( $T_P$  =1450°C). The present  $P_f$  of mantle melting is greater than the Neoproterozoic  $P_f$   
 431 due to the lower  $T_P$ .

432



433

434 **Fig. 2 A pMELTS simulation showing the relation between the alkali index (A.I.)**  
 435 **of melts and temperature-pressure conditions of mantle melting.** The A.I. is  
 436 defined by  $(\text{Na}_2\text{O}+\text{K}_2\text{O})^2/(\text{SiO}_2-38)$ . The major element compositions of the source  
 437 materials were given using the primitive mantle suggested by McDonough and Sun<sup>32</sup>.  
 438 **a.** The isobaric batch melting models of the primitive mantle component with 0.1 wt%  
 439 H<sub>2</sub>O. **b.** The isobaric batch melting models of the primitive mantle component with  
 440 0.3 wt% H<sub>2</sub>O. The grey curves with labels show the values of A.I. **c.** The A.I.  
 441 contours for batch melting models of the primitive mantle component with 0.1 wt%  
 442 H<sub>2</sub>O. **d.** The A.I. contours for batch melting models of the primitive mantle  
 443 component with 0.3 wt% H<sub>2</sub>O. The high A.I. value corresponds to a low-temperature,  
 444 high-pressure condition of mantle melting.



445

446

447

448

449

450

451

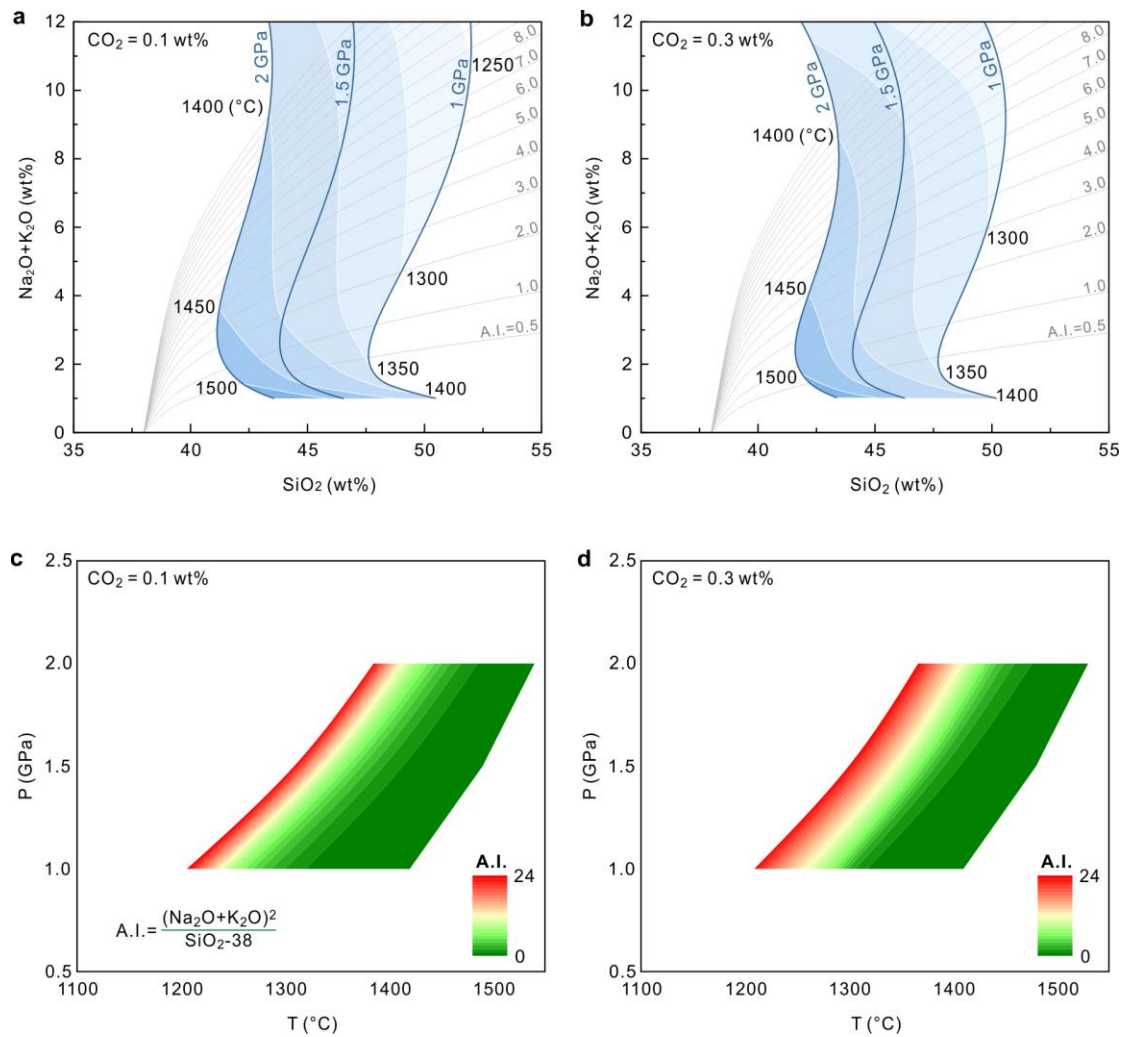
452

453

454

455

**Fig. 3 Secular variations of the compositions of global-scale intracontinental basalts since the Neoproterozoic (1000-0 Ma).** The intracontinental basalts are selected by  $Sr/Y > 25$  since they are mostly generated by high-pressure melting (Supplementary Fig. 3). **a-d.** The secular variations of alkali index (A.I.),  $Na_2O$  and  $K_2O$ ,  $La/Sm$ , and  $Th$ , respectively.  $A.I. = (Na_2O + K_2O)^2 / (SiO_2 - 38)$ . A moving average smoothing has been applied with a 200-Myr sample window. Error bars denote two standard errors of the means (s.e.m.). The light blue vertical columns with a snowflake symbol represent the Snowball Earth event in the Cryogenian ( $\sim 720\text{--}635\text{ Ma}$ )<sup>26</sup>. The grey horizontal dashed lines show the average values before the Cryogenian.



456

457 **Fig. 4 A pMELTS simulation showing the relation between the alkali index (A.I.)**

458 **of melts and temperature-pressure conditions of mantle melting.** The A.I. is

459 defined by  $(\text{Na}_2\text{O} + \text{K}_2\text{O})^2 / (\text{SiO}_2 - 38)$ . The major element compositions of the source

460 are the primitive mantle of McDonough and Sun<sup>32</sup>. **a.** Isobaric batch melting models

461 for the primitive mantle component with 0.1 wt% CO<sub>2</sub>. **b.** The isobaric batch melting

462 models of the primitive mantle component with 0.3 wt% CO<sub>2</sub>. The labelled grey

463 curves show values of A.I. **c.** A.I. contours for batch melting models of the primitive

464 mantle component with 0.1 wt% CO<sub>2</sub>. **d.** A.I. contours for batch melting models of

465 the primitive mantle component with 0.3 wt% CO<sub>2</sub>. A high A.I. value corresponds to

466 mantle melts produced at low-temperature and/or high-pressure. The increase of CO<sub>2</sub>

467 in the mantle peridotite has a negligible influence on the A.I. of the melt, whereas

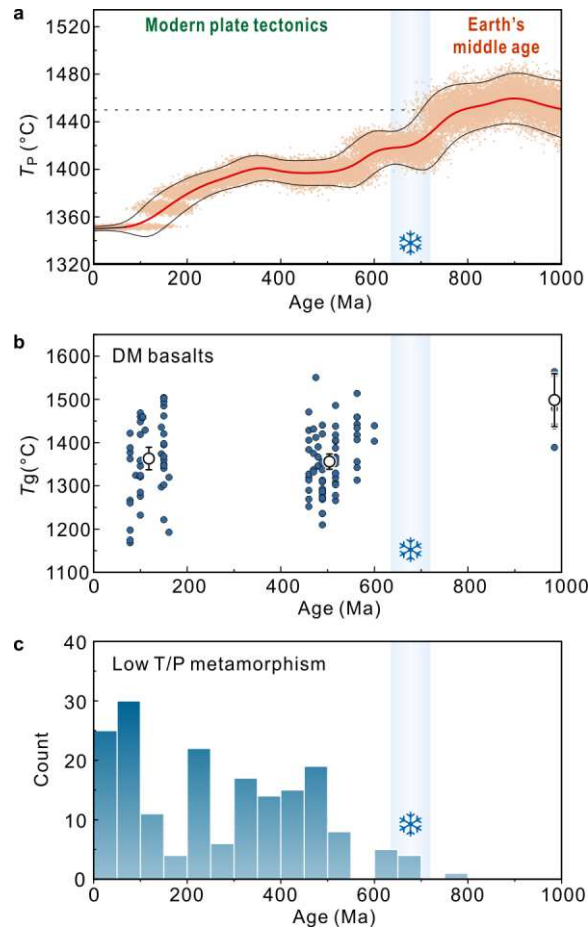
468 decreasing temperature or increasing pressure will dramatically elevate A.I.

469

470

471

472



473

474 **Fig. 5 The thermal evolution model of the mantle.** **a.** The Monto-Carlo simulated  
 475 model of mantle potential temperature ( $T_P$ ) through time using the secular variation of  
 476 A.I. in intracontinental basalts. The horizontal dashed line shows the  $T_P = 1450^{\circ}\text{C}$ . **b.**  
 477 Magma generation temperature ( $T_g$ ) of depleted mantle (DM) basalts. Data are from  
 478 Condie et al.<sup>44</sup>. White circles represent the average  $T_g$  of DM basalts for different  
 479 geological periods. Error bars are 2 s.e.m. **c.** Histograms showing the frequency of  
 480 low thermal gradient ( $T/P$ ) metamorphism through time<sup>2</sup>. The bin size is 50 million  
 481 years.  
 482

# Figures

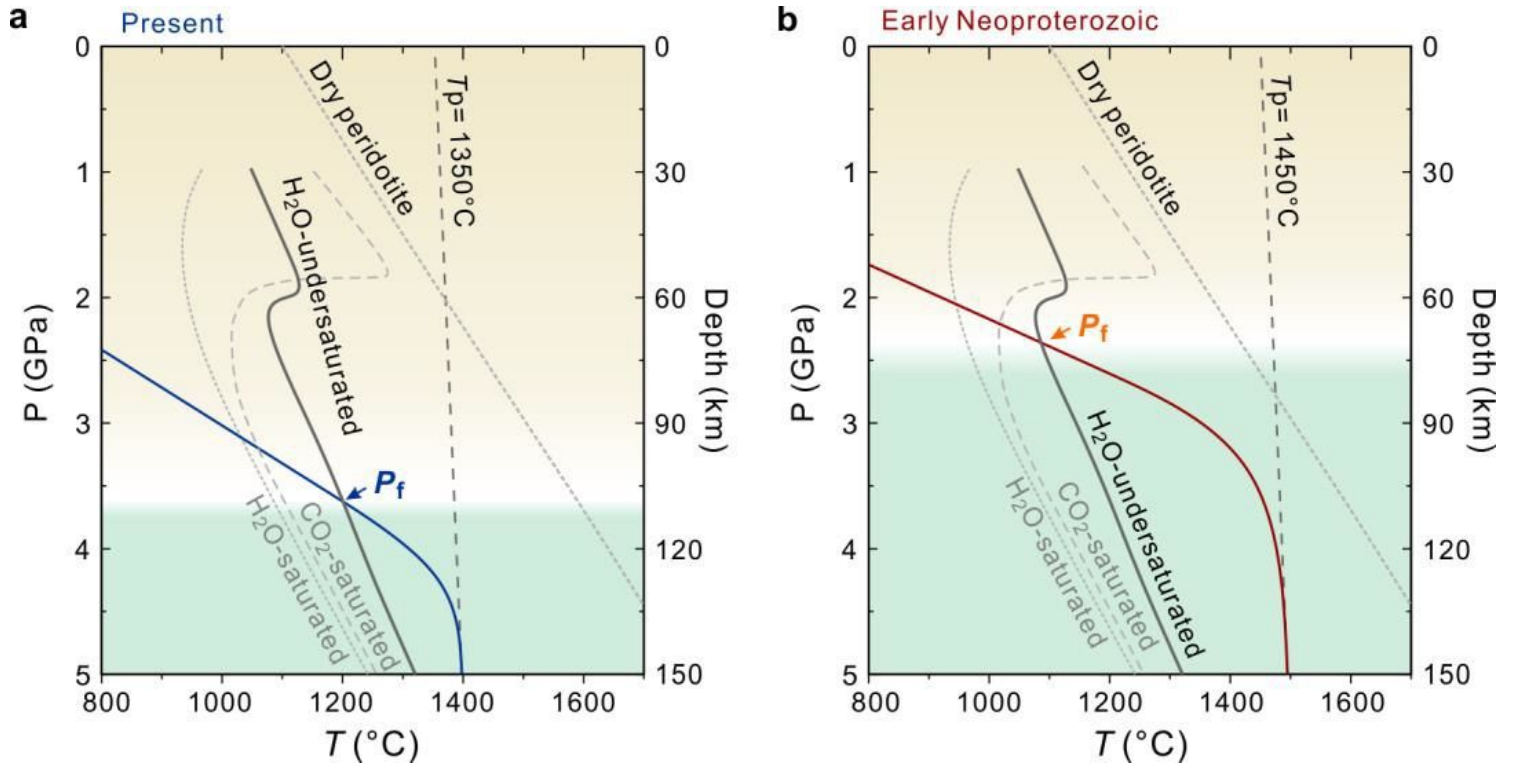
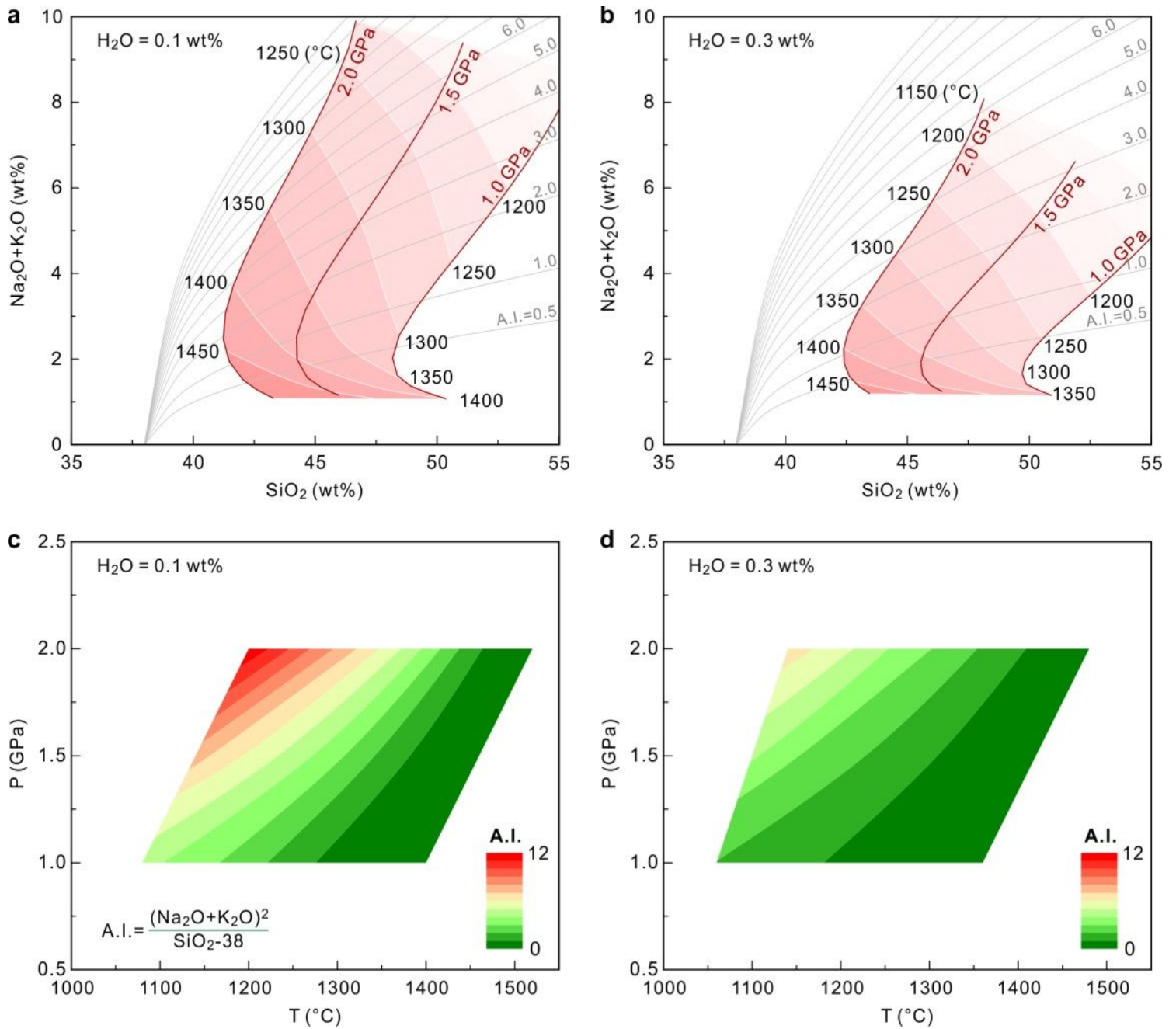


Figure 1

Relation between the pressure of the final melting ( $P_f$ ) of the mantle and the potential temperature ( $T_p$ ) of the adiabatic mantle. The solidus of dry peridotite, H<sub>2</sub>O-undersaturated, H<sub>2</sub>O-saturated and CO<sub>2</sub>-saturated pyrolite39 are shown with their labels. a. A schematic model showing the depth of  $P_f$  at present ( $T_p = 1350^\circ\text{C}$ ). b. A schematic model showing the depth of  $P_f$  in the Early Neoproterozoic ( $T_p = 1450^\circ\text{C}$ ). The present  $P_f$  of mantle melting is greater than the Neoproterozoic  $P_f$  due to the lower  $T_p$ .



**Figure 2**

A pMELTS simulation showing the relation between the alkali index (A.I.) of melts and temperature-pressure conditions of mantle melting. The A.I. is defined by  $(Na_2O+K_2O)^2/(SiO_2-38)$ . The major element compositions of the source materials were given using the primitive mantle suggested by McDonough and Sun<sup>32</sup>. a. The isobaric batch melting models of the primitive mantle component with 0.1 wt% H<sub>2</sub>O. b. The isobaric batch melting models of the primitive mantle component with 0.3 wt% H<sub>2</sub>O. The grey curves with labels show the values of A.I. c. The A.I. contours for batch melting models of the primitive mantle component with 0.1 wt% H<sub>2</sub>O. d. The A.I. contours for batch melting models of the primitive mantle component with 0.3 wt% H<sub>2</sub>O. The high A.I. value corresponds to a low-temperature, high-pressure condition of mantle melting.

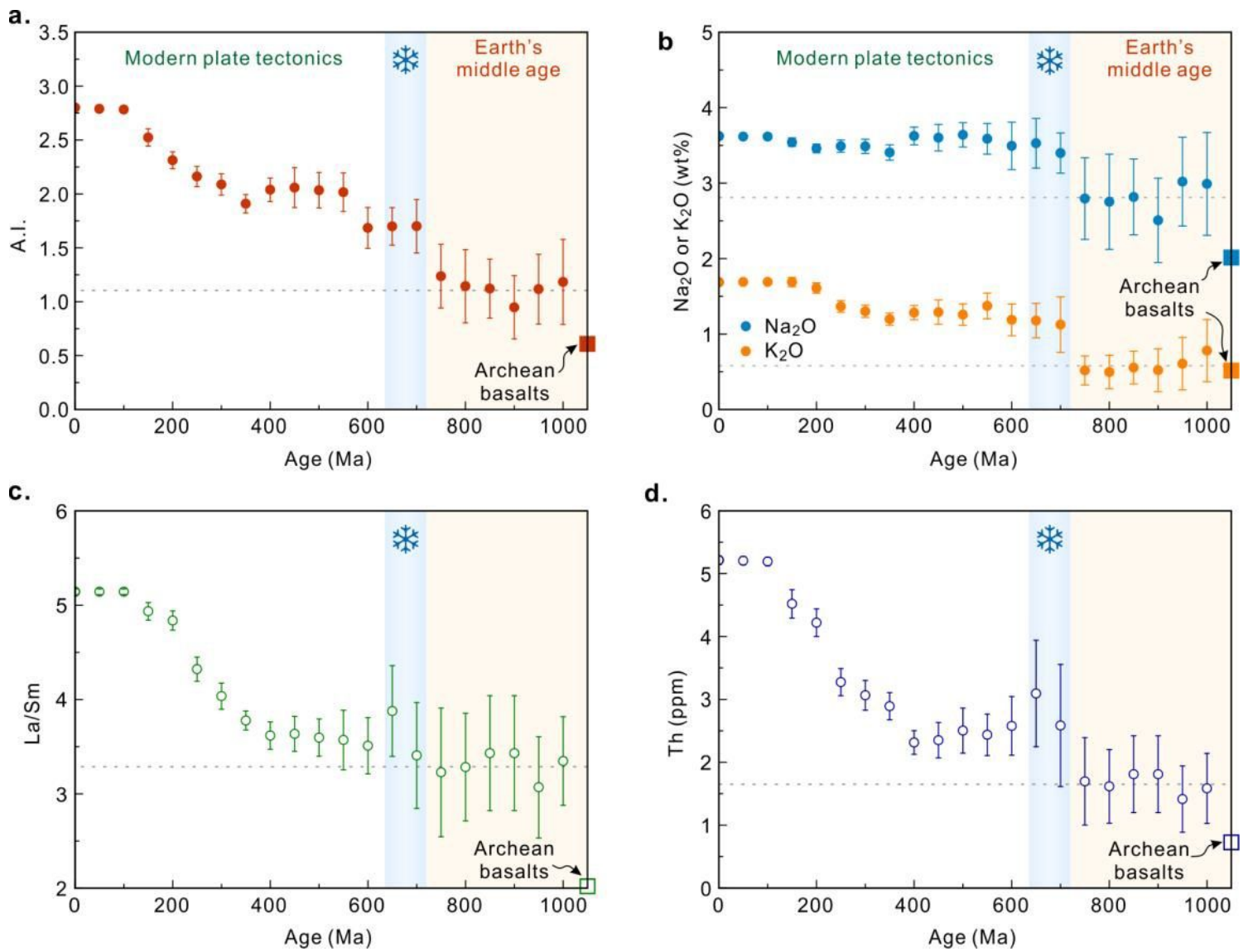


**Figure 3**

Secular variations of the compositions of global-scale intracontinental basalts since the Neoproterozoic (1000-0 Ma). The intracontinental basalts are selected by  $Sr/Y > 25$  since they are mostly generated by high-pressure melting (Supplementary Fig. 3). a-d. The secular variations of alkali index (A.I.), Na<sub>2</sub>O and K<sub>2</sub>O, La/Sm, and Th, respectively.  $A.I. = (Na_2O + K_2O)_2 / (SiO_2 - 38)$ . A moving average smoothing has been applied with a 200-Myr sample window. Error bars denote two standard errors of the means (s.e.m.). The light blue vertical columns with a snowflake symbol represent the Snowball Earth event in the Cryogenian (~720–635 Ma)<sup>26</sup>. The grey horizontal dashed lines show the average values before the Cryogenian.

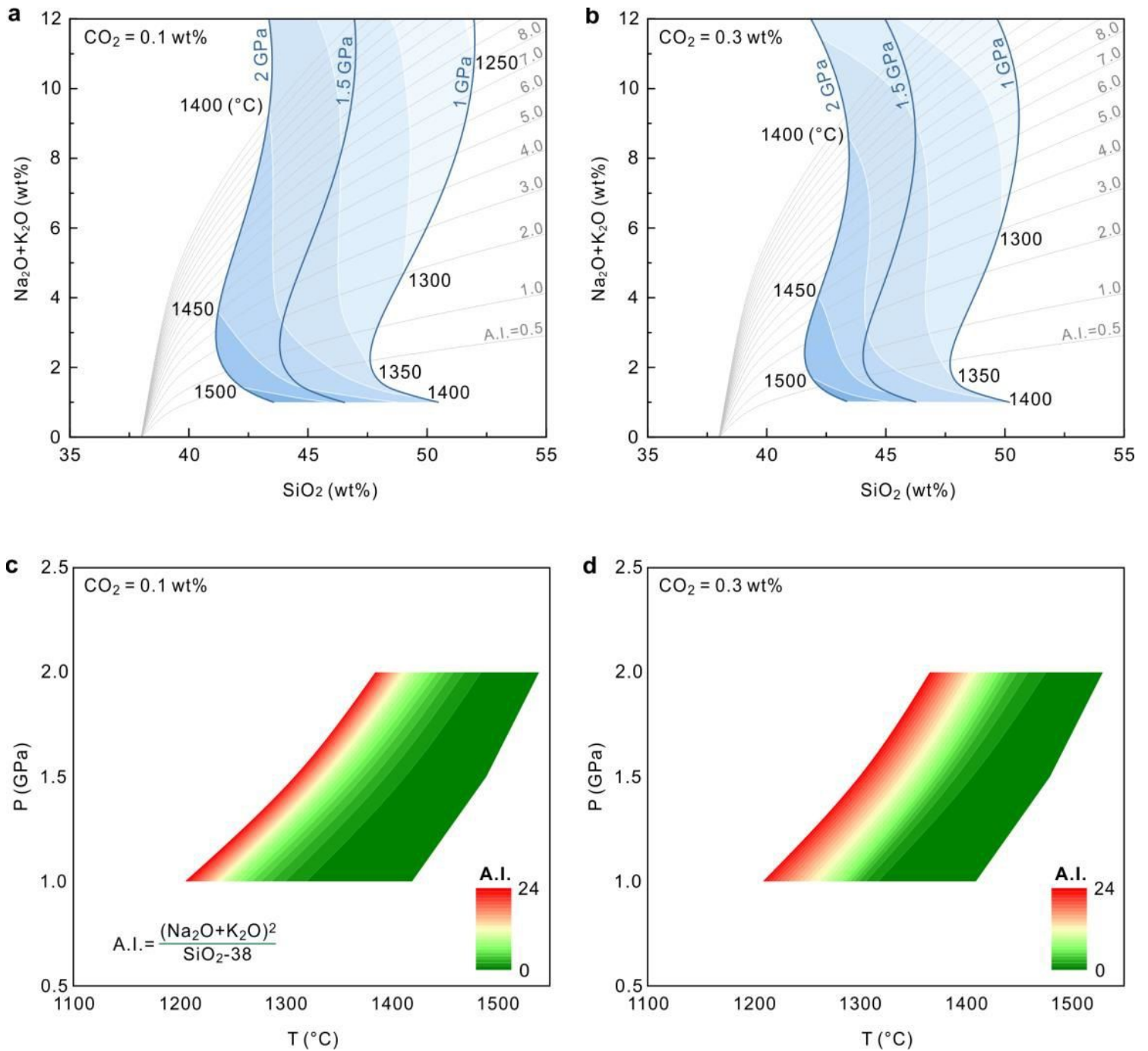


**Figure 4**

A pMELTS simulation showing the relation between the alkali index (A.I.) of melts and temperature-pressure conditions of mantle melting. The A.I. is defined by  $(\text{Na}_2\text{O} + \text{K}_2\text{O})^2 / (\text{SiO}_2 - 38)$ . The major element compositions of the source are the primitive mantle of McDonough and Sun<sup>32</sup>. a. Isobaric batch melting models for the primitive mantle component with 0.1 wt%  $\text{CO}_2$ . b. The isobaric batch melting models of the primitive mantle component with 0.3 wt%  $\text{CO}_2$ . The labelled grey curves show values of A.I. c. A.I. contours for batch melting models of the primitive mantle component with 0.1 wt%  $\text{CO}_2$ . d. A.I. contours for batch melting models of the primitive mantle component with 0.3 wt%  $\text{CO}_2$ . A high A.I. value corresponds to mantle melts produced at low-temperature and/or high-pressure. The increase of  $\text{CO}_2$  in

the mantle peridotite has a negligible influence on the A.I. of the melt, whereas decreasing temperature or increasing pressure will dramatically elevate A.I.

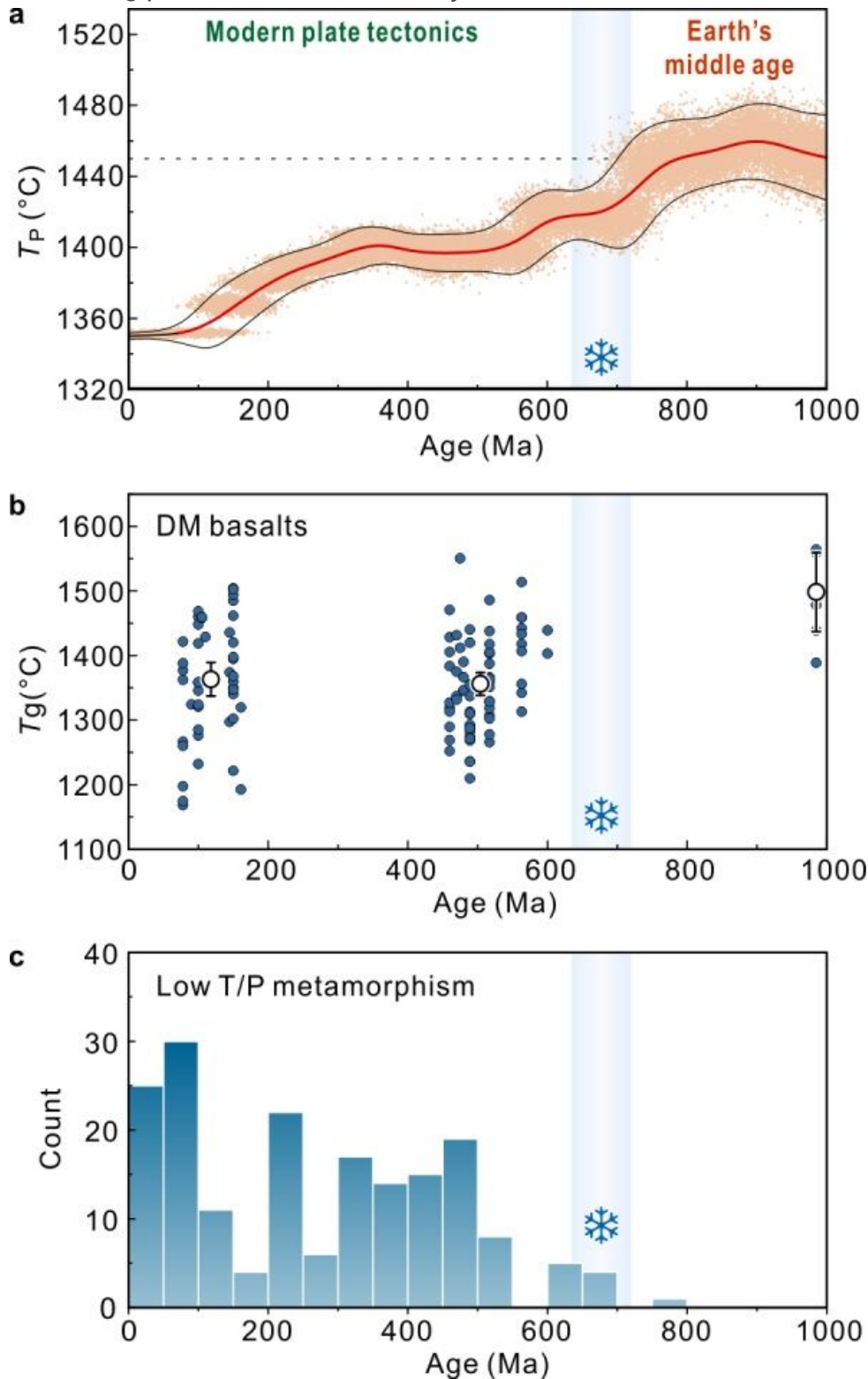


**Figure 5**

The thermal evolution model of the mantle. a. The Monte-Carlo simulated model of mantle potential temperature (TP) through time using the secular variation of A.I. in intracontinental basalts. The horizontal dashed line shows the  $T_P = 1450$   $^{\circ}\text{C}$ . b. Magma generation temperature ( $T_g$ ) of depleted

mantle (DM) basalts. Data are from Condie et al.44. White circles represent the average  $T_g$  of DM basalts for different geological periods. Error bars are 2 s.e.m. c. Histograms showing the frequency of low thermal gradient (T/P) metamorphism through time<sup>2</sup>. The bin size is 50 million years.

## Supplementary Files

This is a list of supplementary files associated with this preprint. Click to download.

- [BSMean.txt](#)
- [MC.txt](#)
- [EarthChemvol.xlsx](#)
- [SourceData.xlsx](#)
- [Supplementary.pdf](#)